

Polarization Spinodal at Ferroelectric Morphotropic Phase Boundary

Xiaoqin Ke,¹ Dong Wang^{1,*}, Xiaobing Ren,^{1,2} and Yunzhi Wang³

¹*Frontier Institute of Science and Technology, MOE Key Laboratory for Nonequilibrium Synthesis and Modulation of Condensed Matter, State Key Laboratory for Mechanical Behavior of Materials, Xi'an Jiaotong University, Xi'an 710049, China*

²*Ferroic Physics Group, National Institute for Materials Science, Tsukuba, 305-0047 Ibaraki, Japan*

³*Department of Materials Science and Engineering, The Ohio State University, Columbus, Ohio 43210, USA*



(Received 24 March 2020; revised 18 June 2020; accepted 20 August 2020; published 14 September 2020)

Here, we report a new phenomenon of uniform and continuous transformation of a single polarization domain into alternating nanodomains of two polarization vectors with the same magnitude but different directions at ferroelectric morphotropic phase Boundary (MPB). The transformation is fully reversible and could enhance the piezoelectric coefficient d_{33} . Further free energy calculations illustrate that such a polarization “decomposition” process occurs within the region on the Landau free energy curve with respect to the polarization direction where the second derivative becomes negative, which is similar to spinodal instability in phase transformations such as spinodal ordering or isostructural phase separation (e.g., spinodal decomposition). This “polarization spinodal” uncovers a new mechanism of polarization switching that may account for the ultrahigh hysteretic piezoelectric strain at the MPB. This work could shed light on the development of phase transition theory and the design of novel ferroelectric memory materials.

DOI: [10.1103/PhysRevLett.125.127602](https://doi.org/10.1103/PhysRevLett.125.127602)

Polarization switching under external fields underpins the “smart” properties of ferroelectric materials such as ferroelectricity and piezoelectricity that have found a wide range of applications in electronic devices such as nonvolatile memories, actuators, and sensors [1–2]. Because of the ultrahigh piezoelectricity ($d_{33} > 4000$ pC/N) achieved in ferroelectrics at the so-called ferroelectric morphotropic phase boundary (MPB) [3], the mechanisms of polarization switching at MPBs have attracted continued interest in recent years. Contrary to the conventional domain wall motion process under an electric field known for most non-MPB ferroelectric materials, polarization switching in MPB ferroelectric materials under an electric field can be realized by polarization rotation through an intermediate monoclinic phase [4–6]. Polarization rotation could occur uniformly within a single domain at MPB due to the small polarization anisotropy [7]. Further studies have shown that such uniform polarization rotation can occur even in pure PbTiO_3 and result in high piezoelectric response if the system is tuned from the single tetragonal phase region to the MPB region by a pressure field [8,9]. However, such a polarization rotation model, originally developed for homogeneous domain switching (i.e., uniform polarization rotation within a domain), cannot account for microstructure evolution from a homogeneous microdomain to heterogeneous nanodomain-in-microdomain (NIM) hierarchical structures frequently observed in experiments [10–13], as well as how this microstructure change influences the piezoelectric property of MPB compositions.

Here by using phase field simulations, we demonstrate a new “polarization spinodal” mechanism for microdomain to NIM structure evolution at MPB, which explains the origin of the heterogeneous NIM structure. The homogeneous microdomain decomposes into alternating nanodomains of two polarization vectors with the same magnitude but different directions through a spinodal instability, which is similar to the conventional spinodal mechanism [14–16]. Within each nanodomain of the NIM structure, uniform polarization rotation under external electric field occurs, but the polarization rotation in alternating nanodomains is not uniform and the nonuniformity occurs through polarization spinodal in terms of polarization directions. Such a polarization spinodal process contributes to further enhancement of d_{33} at ferroelectric MPB.

The model system adopted in the phase field simulations is a ferroelectric solid solution with cubic (C) to tetragonal (T) and cubic (C) to rhombohedral (R) transitions at the two ends $c = 0.0$ and $c = 1.0$ (c is composition), respectively, and a T/R morphotropic phase boundary in between [17–18]. The polarization vector of each domain in the system is represented by \mathbf{P} (P_1, P_2, P_3). The total free energy of the system F_{total} includes the Landau free energy F_{Landau} , the gradient energy F_{gradient} , characterizing the energy caused by polarization inhomogeneity, the long-range elastic strain energy F_{elastic} , and the long-range electrostatic energy F_{electric} , i.e., $F_{\text{total}} = F_{\text{Landau}} + F_{\text{gradient}} + F_{\text{elastic}} + F_{\text{electric}}$. The Landau free energy density f_{Landau} is approximated by a sixth order Landau polynomial of \mathbf{P} (P_1, P_2, P_3):

$$\begin{aligned}
 f_{\text{Landau}} = & \alpha_1 P^2 + \alpha_{11} P^4 + \alpha_{111} P^6 \\
 & + \alpha_{12} (P_1^2 P_2^2 + P_1^2 P_3^2 + P_2^2 P_3^2) + \alpha_{112} [P_1^4 (P_2^2 + P_3^2) \\
 & + P_2^4 (P_1^2 + P_3^2) + P_3^4 (P_1^2 + P_2^2)] + \alpha_{113} P_1^2 P_2^2 P_3^2 \\
 & - E_{1,\text{ap}} P_1 - E_{2,\text{ap}} P_2 - E_{3,\text{ap}} P_3,
 \end{aligned} \quad (1)$$

where $\alpha_1, \alpha_{11}, \alpha_{111}, \alpha_{12}, \alpha_{112}, \alpha_{113}$ are Landau coefficients depending on c and T (temperature), $E_{i,\text{ap}}$ is the applied external electric field, and P is the length of the polarization vector. For simplicity, the gradient energy coefficient is assumed to be isotropic [19–21]. Thus, the gradient energy density f_{gradient} is written in terms of \mathbf{P} as follows: $f_{\text{gradient}} = \frac{1}{2} G_{11} [\sum_{i=1,2,3; j=1,2,3} (P_{i,j})^2]$, where G_{11} is the gradient energy coefficient. The elastic energy density f_{elastic} is calculated by the following equation: $f_{\text{elastic}} = \frac{1}{2} C_{ijkl} e_{ij} e_{kl} = \frac{1}{2} C_{ijkl} (\epsilon_{ij} - \epsilon_{ij}^0) (\epsilon_{kl} - \epsilon_{kl}^0)$, where C_{ijkl} is the elastic constant e_{ij} , ϵ_{ij} , ϵ_{ij}^0 is the elastic strain, total strain, and spontaneous strain, respectively. The spontaneous strain is related to the polarization \mathbf{P} by $\epsilon_{ij}^0 = Q_{ijkl} P_k P_l$, where Q_{ijkl} is the electrostrictive coefficient. The electrostatic energy density is calculated by the following equation: $f_{\text{electric}} = -E_i P_i - \frac{1}{2} E_{i,\text{depol}} \bar{P}_i$, where E_i denotes the inhomogeneous electric field due to the dipole-dipole interactions, $E_{i,\text{depol}}$ is the average depolarization field due to the surface charge, and \bar{P}_i is the average polarization. The temporal evolution of the polarization vector field can be obtained by solving the time-dependent Landau-Ginzburg equation: $[dP_i(x, t)]/dt = -M \{\delta F_{\text{total}} / [\delta P_i(x, t)]\}$, $i = 1, 2, 3$, where M is the kinetic coefficient and t is the time. The parameters used in the calculations are given in Supplemental Material [22]. The simulations were carried out in two dimensions (2D) with cell sizes 512×512 grids with periodic boundary conditions in all dimensions. The time-dependent Landau-Ginzburg equation was solved by the semi-implicit Fourier spectral method [20].

Figure 1 shows the evolution of domain structure upon applying and removing an electric field ($E_{1,\text{ap}}$) to a [10]-poled single crystal with composition $c = 0.51$ at $T = 15^\circ\text{C}$, which is close to the MPB of the model system [17–18]. It is seen that at $E_{1,\text{ap}} = 0$, the sample exhibits a nanodomain-in-microdomain (NIM) structure [Fig. 1(a1)]. Such NIM structures have been reported both in experiments [12,26] and in simulations [17–18]. However, the mechanism underlying the formation of these NIM structures was not revealed and the related piezoelectric response was unclear. Upon applying an electric field, such NIM structure transforms to a microdomain structure [Figs. 1(a3) and 1(a4)]. The microdomain structure then transforms back to the NIM structure [Figs. 1(a7) and 1(a8)] upon removal of the electric field. Figures 1(b1) and 1(b2) give the variation of θ [the angle between the polarization vector $\mathbf{P}(P_1, P_2)$ and the horizontal axis,

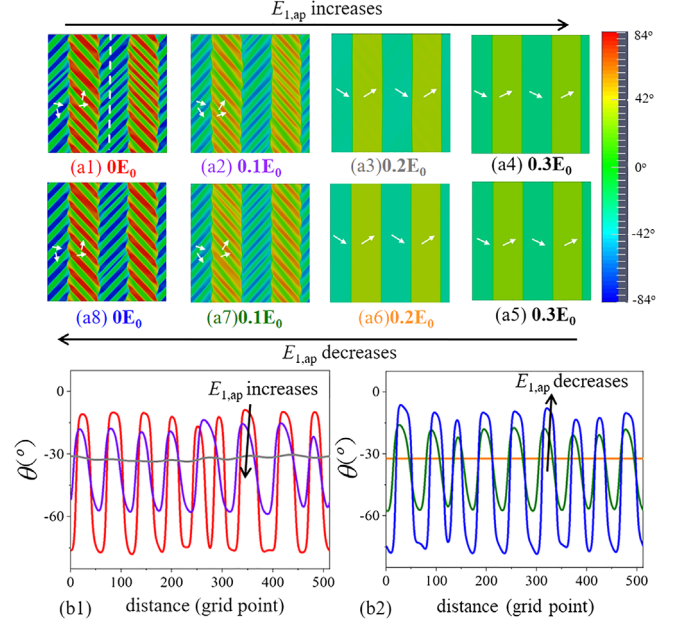


FIG. 1. (a1)–(a8) Reversible nanodomain-in-microdomain (NIM) to microdomain transformation upon applying and removing $E_{1,\text{ap}}$ on an MPB sample. (b1) Variation of θ along the dashed line in Fig. 1(a1) upon increasing $E_{1,\text{ap}}$ from 0 (a1) to $0.2E_0$ (a3). (b2) Variation of θ along the dashed line upon decreasing $E_{1,\text{ap}}$ from $0.2E_0$ (a6) to 0 (a8).

$\theta = \arctan(P_2/P_1)$] along the dashed line upon increasing $E_{1,\text{ap}}$ from 0 to $0.3E_0$ [$E_0 \sim 250$ kV/cm, Figs. 1(a1)–(a4)] and upon decreasing $E_{1,\text{ap}}$ from $0.3E_0$ to 0 [Figs. 1(a5)–1(a8)], respectively. It shows that upon increasing $E_{1,\text{ap}}$ [Fig. 1(b1)], the two polarization vectors gradually rotate toward each other until they merge into one polarization vector. Note that the volume fraction of each nanodomain remains almost constant during this NIM to microdomain transition process. Upon decreasing $E_{1,\text{ap}}$ [Fig. 1(b2)], the single polarization vector of the microdomain decomposes into two polarization vectors in the form of alternating polarization nanodomains. These two vectors gradually rotate away from each other with further decreasing $E_{1,\text{ap}}$, which is a reverse process of the polarization switching from NIM to microdomain structure upon increasing $E_{1,\text{ap}}$. By comparing the microstructures in Figs. 1(a1)–1(a8) and the polarization profiles in Figs. 1(b1)–1(b2), it is clear that the NIM to microdomain transition is highly reversible. Our simulations are consistent with the experimental observations that nanodomains appear at small electric fields and disappear at large electric fields [11,12,27]. Furthermore, the width of the nanodomains in the NIM structure of Fig. 1 is ~ 60 nm, which is within the range of 10 – 500 nm observed in experiments for PMN- x Pt near MPB compositions [26,28,29]. The nanodomains in the NIM structure have been identified as a monoclinic (M) phase whose polarization vector can rotate within a plane giving a wide range of possible θ values [12,28].

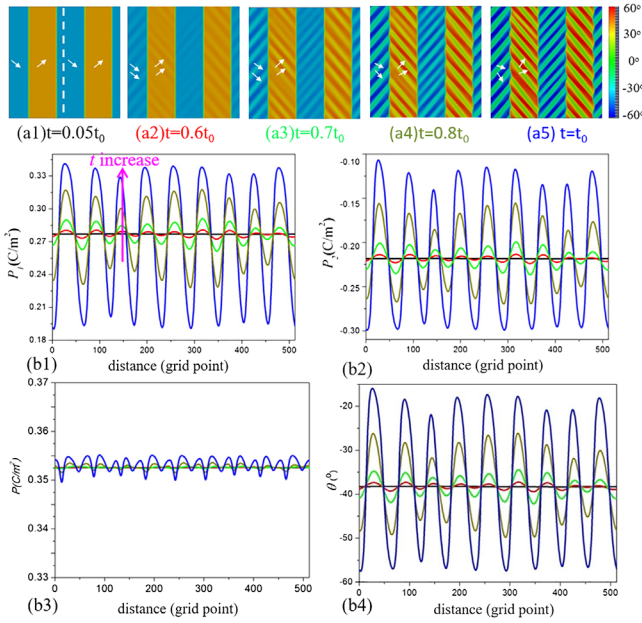


FIG. 2. Polarization spinodal mechanism for the microdomain to nanodomain-in-microdomain (NIM) transformation at $E_{1,ap} = 0.1E_0$ for the sample (a1)–(a5). Domain structure change with t . (b1)–(b4) Variation of P_1 , P_2 , P , and θ along the dashed line in (a) with t .

To further examine how one microdomain of single polarization decomposes into alternating nanodomains of two different polarizations upon decreasing the electric field described in Fig. 1, we plot the domain structure evolution with time (t) at $E_{1,ap} = 0.1E_0$ starting from the microdomain structure, which is illustrated in Figs. 2(a1)–2(a5). Besides, the change of polarization components P_1 and P_2 along the dashed line in Fig. 2(a1) with time is given in Figs. 2(b1) and 2(b2), respectively. It is readily seen that in the initial stage [for example, at $t = 0.6t_0$, Fig. 2(a2)], nanodomains of two different polarizations appear simultaneously and homogeneously throughout the entire parent microdomain, but the polarization components (P_1 and P_2) of the nanodomains at $t = 0.6t_0$ deviate only slightly from that of the microdomain at $t = 0.05t_0$ shown in Fig. 2(a1). The deviation increases gradually with time and finally the polarizations in the nanodomains reach equilibrium at t_0 (when no further change with time could be detected), as shown in Figs. 2(a1)–2(a5). t_0 is $\sim 2 \times 10^{-8}$ s [22], which might be too short to observe the related microstructural evolution in experiments [28].

The large extent and small degree of polarization variation at the initial stage (for example, at $t = 0.6t_0$) suggest that the microdomain to nanodomain transition occurs through a mechanism different from the conventional nucleation and growth mechanism. This is because, for nucleation and growth, the polarization variation at the initial stage should be large in degree and small in extent. It resembles the spinodal decomposition or spinodal ordering

mechanism where the variation of concentration or long-range order parameter at the initial stage is small in degree and large in extent [14–16]. Therefore, we refer to this continuous polarization decomposition process as polarization spinodal in parallel to composition spinodal. The order parameter that characterizes the decomposition process is polarization in the former and concentration for the latter.

To further characterize the continuous transition characteristics of the polarization spinodal, we plot in Figs. 2(b3) and 2(b4) the change of P ($P = \sqrt{P_1^2 + P_2^2}$) and θ along the dashed line in Fig. 2(a1). It is readily seen that P hardly changes while θ changes gradually with time. Thus, the polarization spinodal mechanism during the microdomain to NIM transformation can be described as a microdomain with a uniform polarization \mathbf{P}_0 decomposing into alternating nanodomains with two different polarization vectors, \mathbf{P}_A and \mathbf{P}_B , both of which differ from \mathbf{P}_0 mainly in the vector direction but not in the magnitude. Artemev *et al.* have found that polarization spinodal in terms of polarization magnitude could occur in ferroelectric thin films with large depolarization field [30–31]. It is expected that polarization spinodal decomposition in terms of both magnitude and direction could occur in thin films with composition at MPB.

Next, we analyze why the microdomain decomposes into alternating nanodomains from $E_{1,ap} = 0.2E_0$ to $E_{1,ap} = 0.1E_0$ by a spinodal mechanism. Figures 3(a)–3(d) show the Landau free energy curves as a function of polarization angle θ at $E_{1,ap} = 0.3E_0$, $0.2E_0$, $0.1E_0$, and 0, respectively. The polarization angles of different domains appearing at these electric fields are indicated by the circles (filled with different colors) on the free energy curves. It is seen that at $E_{1,ap} = 0.3E_0$, the lowest Landau free energy occurs at $\theta = 0$. However, the equilibrium polarization of the microdomains at this electric field is not at $\theta = 0$, but at $\theta = -26^\circ$ and $\theta = 26^\circ$. The deviation of θ from the one given by the minimum Landau free energy is due to the elastic strain energy and electrostatic energy contributes as reported in Ref. [17]. Although the local position of \mathbf{P} is not at the minimum Landau free energy position, the total free energy of the system is at its minimum. Decreasing $E_{1,ap}$ from $0.3E_0$ to $0.2E_0$, θ of the microdomain rotates from $\pm 26^\circ$ to $\pm 31^\circ$. Upon further decreasing $E_{1,ap}$ from $0.2E_0$ to $0.1E_0$, θ continues to rotate from $\pm 31^\circ$ to $\pm 38^\circ$. Up to now, the polarization switching process follows what the polarization rotation model predicts. However, as seen in Fig. 3(c), $\theta = -38^\circ$ and $\theta = 38^\circ$ are located in the spinodal region of the Landau free energy where $f''_{\text{Landau}} < 0$. As a result, both polarizations with $\theta = -38^\circ$ and $\theta = 38^\circ$ in the microdomains decompose spontaneously into two polarizations $\sim 20^\circ$ away from the parent domain polarization direction (for example, θ decomposes into $\pm 18^\circ$ and $\pm 58^\circ$ from $\pm 38^\circ$) leading to the NIM structure. When decreasing $E_{1,ap}$ from $0.1E_0$ to 0, it can be seen that θ further rotates to

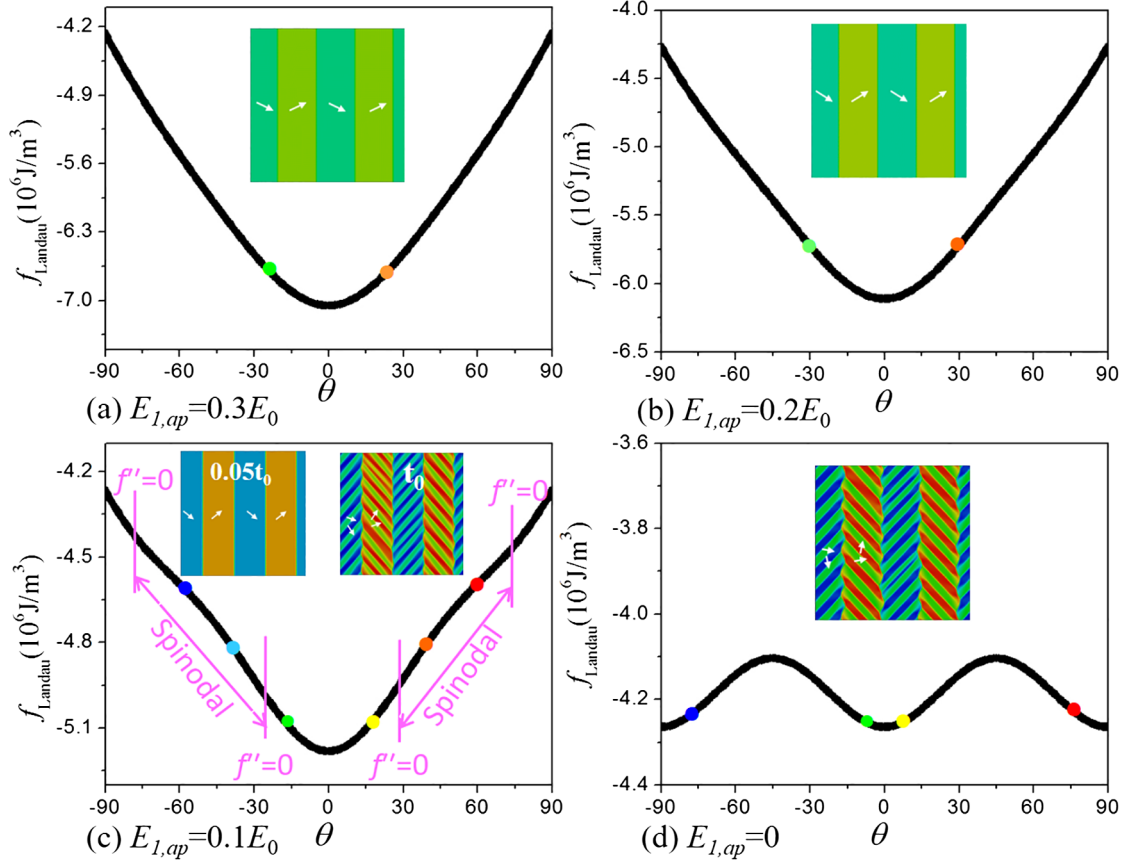


FIG. 3. The change of Landau free energy with polarization direction at (a) $E_{1,ap} = 0.3E_0$; (b) $E_{1,ap} = 0.2E_0$; (c) $E_{1,ap} = 0.1E_0$; and (d) $E_{1,ap} = 0$.

the values closer to 0° or 90° to minimize the Landau free energy. The above Landau free energy analysis suggests that as long as the polarization of the microdomain is located in the spinodal region of the Landau free energy curve, polarization spinodal could occur. Further mathematical analysis giving a critical external electric field below which the polarization spinodal instability may occur, a critical wavelength (λ_c) above which polarization waves will be stable and a wavelength with the maximum growth speed is provided in the Supplemental Material [22].

The spinodal region given in Fig. 3 is calculated from the Landau free energy. However, the total free energy of the system also includes elastic, electrostatic, and gradient energies. The calculated four different free energy terms (F_{elastic} , F_{electric} , F_{gradient} , and F_{Landau}) as well as the total free energy (F_{total}) of the microdomain structure (4M) and the NIM structure shown in Figs. 2(a1) and 2(a5) are shown in Supplemental Material [22]. It is seen that although F_{elastic} and F_{electric} increase by a small amount for the NIM structure as compared to the 4M structure, F_{Landau} decreases by a larger amount and thus F_{total} is reduced for the NIM structure. In other words, the NIM structure has decreased F_{Landau} as illustrated in Fig. 3, which can

compensate for the small increase in F_{elastic} and F_{electric} and thus leads to a decrease in F_{total} . Therefore, for the microdomain to NIM transition, decreasing in F_{Landau} plays the dominant role in the F_{total} and the spinodal region in F_{Landau} curve can approximately determine whether the polarization spinodal process occurs or not as given in Fig. 3. Note that the polarization spinodal mechanism is the operating phase transition mechanism when the free energy as a function of polarization direction θ is concave down ($f''_{\text{Landau}} < 0$), while the traditional nucleation and growth mechanism is the operating phase transition mechanism when the free energy as a function of polarization direction θ is concave up ($f''_{\text{Landau}} > 0$).

The strain (S)–electric field (E) loop of the microstructures shown in Figs. 1(a1)–1(a8) is calculated and shown in Fig. 4. The S – E loop is nearly hysteresis free, which is consistent with the experiments [32,33]. The hysteresis-free character of the S – E loop can be attributed to the nearly reversible polarization spinodal process as shown in Fig. 1. Upon increasing the electric field, the polarization vectors in the nanodomains gradually rotate toward the field direction until the two vectors coalesce into a single one (Fig. 1). The single polarization vector in the microdomain then goes through a pure polarization rotation

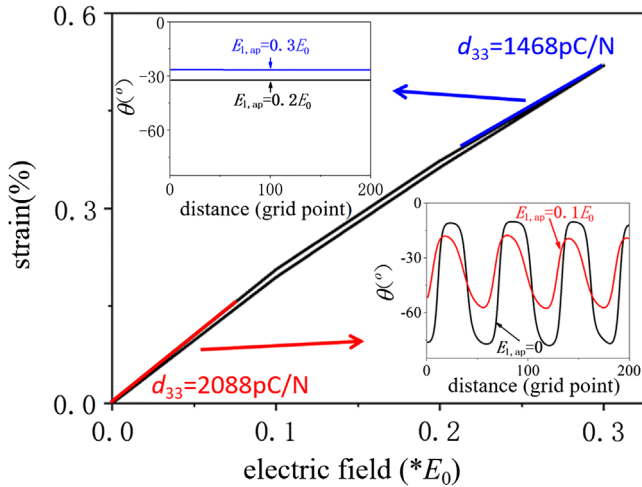


FIG. 4. (a) S – E loop of single crystal upon increasing and decreasing electric field during the process shown in Fig. 1. The inset figures show variation of θ along part of the dashed line in Fig. 1(a1) upon decreasing $E_{1,ap}$ from $0.3E_0$ to $0.2E_0$ and upon increasing $E_{1,ap}$ from 0 to $0.1E_0$, respectively.

process upon further increasing the electric field to $0.3E_0$ (Fig. 1). By calculating d_{33} from the slope of S – E loop at different electric fields, it can be seen that d_{33} is much larger at $E_{1,ap} = 0$ (2088 pC/N) than that at $E_{1,ap} = 0.3E_0$ (1468 pC/N). Li *et al.* have reported larger d_{33} at small fields than that at higher fields at the MPB of $\text{PbMg}_{1/3}\text{Nb}_{2/3-x}\text{PbTiO}_3$ system [34], which supports our simulations. The insets in Fig. 4 give the change of polarization vector along the dashed line in Fig. 1(a1) when changing the electric field at $E_{1,ap} = 0.3E_0$ and $E_{1,ap} = 0$, respectively. It is seen that the degree of polarization rotation is much larger at $E_{1,ap} = 0$ than that at $E_{1,ap} = 0.3E_0$. Such results suggest that the nanodomains induced by the polarization spinodal mechanism can ease polarization rotation under the electric field and thus increase d_{33} as compared to the microdomains.

The necessary condition for polarization spinodal in terms of polarization direction (θ) to occur here is that the polarization direction (θ) of the microdomain locates in the spinodal region where the second derivative of the Landau free energy becomes negative. Thus, the polarization anisotropy has to be small, otherwise the θ value of the microdomain would go to the minimum Landau free energy position because deviating from this position would increase the Landau free energy by a relatively large amount. Therefore, the anisotropic coefficients ($\alpha_{12}, \alpha_{112}, \alpha_{123}$) in the Landau free energy given in Eq. (1) have to be small. This is why the polarization spinodal decomposition process could only occur in a composition range near the MPB of the model system studied [22]. In addition, if there are defects or surfaces, for example, in relaxor ferroelectric MPB systems [35,36], then polarization spinodal may occur first at these defects

[37]. Also, 3D simulations show a similar polarization spinodal process at the MPB composition [22]. Large-scale atomistic simulations with newly developed reactive potentials for ferroelectrics materials [38,39] could be carried out to confirm the generality of the polarization spinodal mechanism.

The polarization spinodal mechanism found in this work may resolve a long-standing controversy on the origin of large piezoelectricity at MPB, i.e., whether the superior piezoelectricity originates from intrinsic contribution (polarization rotation) or extrinsic contribution (domain wall motion) [4,5,18,40,41]. Our work here unambiguously illustrates that domain wall motion hardly occurs during the whole domain switching process even for the nanodomain-in-microdomain structure at ferroelectric MPB and thus suggests that the superior piezoelectricity at ferroelectric MPB is mainly attributed to the intrinsic contributions rather than extrinsic ones.

In conclusion, the nanodomain-in-microdomain (NIM) structure at ferroelectric MPB forms through uniform and continuous transformation of a single polarization domain into alternating nanodomains of two polarization vectors. Such a polarization spinodal process is reversible under the external electric field cycle. The polarization spinodal decomposition process occurs within the region on the Landau free energy curve where the second derivative becomes negative, which is similar to conventional spinodal instability. The piezoelectric response of each single domain in both the microdomain and the NIM structures at MPB regions can be described by polarization rotation. However, the polarization rotation in the alternating nanodomain of the NIM structure at low fields is not uniform but rather occurs by polarization spinodal in terms of polarization directions upon decreasing fields and its reverse process upon increasing fields. Such a polarization spinodal process leads to further enhancement of d_{33} at low fields at MPB. The polarization spinodal model could complete the theory for polarization switching mechanism at ferroelectrics MPB.

X. K., D. W., and X. R. acknowledge the National Natural Science Foundation of China (Grants No. 51802249, No. 51671156, No. 51931004, and No. 51831006), “H2” High-Performance Cluster of XJTU. X. R. acknowledges the financial support from JSPS Kakenhi. Y. W. acknowledges the U.S. Natural Science Foundation (Grant No. DMR-1923929).

*Corresponding author.

wang_dong1223@mail.xjtu.edu.cn

[1] K. Uchino, *Ferroelectric Devices* 2nd ed. (CRC Press, Boca Raton, 2009), <https://doi.org/10.1201/b15852>.

[2] M. Davis, *J. Electroceram.* **19**, 25 (2007).

- [3] C. Qiu, B. Wang, N. Zhang, S. Zhang, J. Liu, D. Walker, Y. Wang, H. Tian, T. R. Shrout, Z. Xu, L.-Q. Chen, and F. Li, *Nature (London)* **577**, 350 (2020).
- [4] H. Fu and R. E. Cohen, *Nature (London)* **403**, 281 (2000).
- [5] R. Guo, L. E. Cross, S-E. Park, B. Noheda, D. E. Cox, and G. Shirane, *Phys. Rev. Lett.* **84**, 5423 (2000).
- [6] Y. Gao, S. A. Dregia, and Y. Wang, *Acta Mater.* **127**, 438 (2017).
- [7] Z. Kutnjak, J. Petzelt, and R. Blinc, *Nature (London)* **441**, 956 (2006).
- [8] M. Ahart, M. Somayazulu, R. E. Cohen, P. Ganesh, P. Dera, H.-K. Mao, R. J. Hemley, Y. Ren, P. Liermann, and Z. Wu, *Nature (London)* **451**, 545 (2008).
- [9] P. Ganesh and R. E. Cohen, *J. Phys. Condens. Matter* **21**, 064225 (2009).
- [10] Z. Chen, L. Hong, F. Wang, S. P. Ringer, and L.-Q. Chen, H. Luo and X. Liao, *Phys. Rev. Lett.* **118**, 017601 (2017).
- [11] R. Theissmann, L. A. Schmitt, J. Kling, R. Schierholz, K. A. Schönau, H. Fuess, and M. Knapp, *J. Appl. Phys.* **102**, 024111 (2007).
- [12] T. Asadaand and Y. Koyama, *Phys. Rev. B* **75**, 214111 (2007).
- [13] J. Gao, D. Xue, Y. Wang, D. Wang, L. Zhang, H. Wu, S. Guo, H. Bao, C. Zhou, W. Liu, S. Hou, G. Xiao, and X. Ren, *Appl. Phys. Lett.* **99**, 092901 (2011).
- [14] J. W. Gibbs, *Collected Works* (Yale University Press, New Haven, Connecticut, 1948), Vol. 1, pp. 105–115, 252–258.
- [15] J. Cahn, *Acta Mater.* **9**, 795 (1961).
- [16] Y. Ni and A. M. Khachaturyan, *Nat. Mater.* **8**, 410 (2009).
- [17] X. Q. Ke, D. Wang, X. Ren, and Y. Wang, *Phys. Rev. B* **88**, 214105 (2013).
- [18] X. Q. Ke, D. Wang, and Y. Wang, *Appl. Phys. Lett.* **108**, 012904 (2016).
- [19] S. Rudraraju, A. Van der Ven, and K. Garikipati, *npj Comput. Mater.* **2**, 16012 (2016).
- [20] S. Choudhury, Y. L. Li, C. E. Krill, III, and L.-Q. Chen, *Acta Mater.* **53**, 5313 (2005).
- [21] W.-F. Rao, M. Wuttig, and A. G. Khachaturyan, *Phys. Rev. Lett.* **106**, 105703 (2011).
- [22] See Supplemental Material at <http://link.aps.org/supplemental/10.1103/PhysRevLett.125.127602> for parameters used in our simulations; the composition range for polarization spinodal; the mathematical analysis of the critical external field below which the polarization spinodal instability may occur, the critical polarization wavelength (λ_c) above which polarization modulations become stable, the wavelength (λ_m) with the maximum growth rate; and 3D simulation results, which includes Refs. [23–25].
- [23] J. Hlinka, *Ferroelectrics* **349**, 49 (2007).
- [24] F. Xue, Y. Ji, and L.-Q. Chen, *Acta Mater.* **133**, 147 (2017).
- [25] S. M. Allen and J. W. Cahn, *Acta Mater.* **27**, 1085 (1979).
- [26] K. Morozumi, J. Kato, Y. Kawakubo, and S. Denda, *Jpn. J. Appl. Phys.* **45**, 6365 (2006).
- [27] M. Otonicar, J. Park, M. Logar, G. Esteves, J. L. Jones, and B. Jancar, *Acta Mater.* **127**, 319 (2017).
- [28] Y. Sato, T. Hirayama, and Y. Ikuhara, *Phys. Rev. Lett.* **107**, 187601 (2011).
- [29] F. Bai, J. Li, and D. Viehland, *Appl. Phys. Lett.* **85**, 2313 (2004).
- [30] A. Artemev and A. Roytburd, *Acta Mater.* **58**, 1004 (2010).
- [31] A. M. Bratkovsky and A. P. Levanyuk, *Appl. Phys. Lett.* **89**, 253108 (2006).
- [32] S.-E. Park and T. R. Shrout, *J. Appl. Phys.* **82**, 1804 (1997).
- [33] M. Davis, D. Damjanovic, and N. Setter, *Phys. Rev. B* **73**, 014115 (2006).
- [34] F. Li, S. Zhang, Z. Xu, X. Wei, J. Luo, and T. R. Shrout, *J. Appl. Phys.* **108**, 034106 (2010).
- [35] D. Phelan, C. Stock, J. A. Rodriguez-Rivera, S. Chi, J. Leao, X. Long, Y. Xie, A. A. Bokov, Z.-G. Ye, P. Ganesh, and P. M. Gehring, *Proc. Natl. Acad. Sci. U.S.A.* **111**, 1754 (2014).
- [36] P. Ganesh, E. Cockayne, M. Ahart, R. E. Cohen, B. Burton, R. J. Hemley, Y. Ren, W. Yang, and Z.-G. Ye, *Phys. Rev. B* **81**, 144102 (2010).
- [37] Y. Lu, C. Wang, Y. Gao, R. Shi, X. Liu, and Y. Wang, *Phys. Rev. Lett.* **109**, 086101 (2012).
- [38] K. P. Kelley, D. E. Yilmaz, L. Collins, Y. Sharma, H. N. Lee, D. Akbarian, A. C. T. van Duin, P. Ganesh, and R. K. Vasudevan, *Phys. Rev. Mater.* **4**, 024407 (2020).
- [39] D. Akbarian, D. E. Yilmaz, Y. Cao, P. Ganesh, I. Dabo, J. Munro, R. V. Ginshovenand, and A. C. T. van Duin, *Phys. Chem. Chem. Phys.* **21**, 18240 (2019).
- [40] Y. M. Jin, Y. U. Wang, A. G. Khachaturyan, J. F. Li, and D. Viehland, *Phys. Rev. Lett.* **91**, 197601 (2003).
- [41] J. Gao, X. Hu, L. Zhang, F. Li, L. Zhang, Y. Wang, Y. Hao, L. Zhong, and X. Ren, *Appl. Phys. Lett.* **104**, 252909 (2014).